Separation of CTCs from WBCs using DEP-assisted inertial manipulation: A numerical study

Mohammed Raihan Uddin[1], Md Tanbir Sarowar[1], and Xiaolin Chen[1*]

[1]School of Engineering and Computer Science, Washington State University, Vancouver, WA 98686
[*]Corresponding author email: chenx@wsu.edu

Keywords:
Label-free separation, Inertial microfluidics, Dielectrophoresis, Circulating tumor cells, High-throughput.

ABSTRACT

Isolation and detection of circulating tumor cells (CTCs) hold significant importance for early diagnosis of cancer and assessment of therapeutic strategies. However, the scarcity of CTCs among peripheral blood cells presents a major challenge to their detection. Additionally, a similar size range between CTCs and white blood cells (WBCs) makes conventional microfluidic platforms inadequate for the isolation of CTCs. To overcome these challenges, in this study, a novel inertial-dielectrophoretic microfluidic channel for size-independent, single-stage separation of CTCs from WBCs has been presented. The proposed device utilizes a spiral microchannel embedded with interdigitated electrodes. A numerical model is developed and validated to investigate the influence of various parameters related to the channel design, fluid flow, and electrode configuration. It was found that optimal separation of CTCs could be obtained at a relatively low voltage, termed critical voltage. Furthermore, at the critical voltage of 7.5V, the hybrid microchannel is demonstrated to be capable of separating CTCs from different WBC subtypes, including Granulocytes, Monocytes, T-lymphocytes, and B-lymphocytes. The unique capabilities of the hybrid spiral microchannel allow for this size-independent isolation of CTCs from a mixture of WBCs. Overall, the proposed technique can be readily utilized for continuous and high-throughput separation of cancer cells.

1 INTRODUCTION

Cancer ranks as the second leading cause of death in the world. According to cancer statistics reports, approximately 610,000 cancer-related fatalities occurred in the US in 2023, amounting to nearly 1,670 deaths per day [1]. A staggering 90% of these deaths can be attributed to the metastasis of cancer cells, facilitated by a specific cell type called Circulating Tumor Cells (CTCs). CTCs possess the ability to extravasate and subsequently function as progenitors for the development of metastatic tumors in remote organs [2]. Additionally, CTCs preserve the heterogeneity and characteristics of the originating tumor. This preservation enables them to serve as essential clinical biomarkers for monitoring cancer progression. Consequently, the detection of CTCs is critical in the diagnosis and treatment of cancer [3]. However, the task of isolating CTCs is fraught with challenges, given their extreme scarcity in bloodstreams, with concentrations ranging from 1 to 10 CTCs per milliliter of whole blood (approximately 1 CTCs per 10^7 white blood cells) in patients with metastatic diseases [4]. Additionally, the considerable size overlap between CTCs and normal blood cells further complicates the separation process. Despite these obstacles, the critical association between cancer metastasis and CTCs underscores the importance of CTC research for applications such as early cancer detection and treatment. As a result, an extensive body of studies has emerged in recent years aimed at devising innovative methods for capturing CTCs within the bloodstream.

Remarkable progress in microfluidics has facilitated the development of many new devices for the characterization and sorting of cells without the need for exogenous labels. These label-free cell sorting devices allow for the examination and utilization of cell attributes, such as size, deformability, magnetic characteristics, dielectric properties, or a combination of these attributes, which are unattainable through biological labeling [5]. Label-free cell separation is also simpler, cheaper, and more efficient compared to the labeled approach [6]. These label-free cell separation methods can be categorized into active and passive techniques, depending on the dominant manipulating force. Active techniques, including dielectrophoresis (DEP), optical tweezers, acoustophoresis, and magnetophoresis, utilize external force fields for the manipulation of particles. These methods enable precise control over cell trajectories and real-time adjustments of their positions. However, active techniques suffer from low throughput, as the external force field must surpass the hydrodynamic force to achieve effective separation [7].

Conversely, passive microfluidic devices, such as inertial microfluidics, field flow fractionation (FFF), deterministic lateral displacement (DLD), and hydrophoresis, rely on the microchannel structure and the intrinsic hydrodynamic forces. Passive microfluidics has the advantages of simple structure, robustness, and high throughput [8]. Inertial microfluidics has emerged as a highly promising passive, label-free separation method and garnered significant interest due to its high throughput capabilities and its significant potential for point-of-care testing applications. First observed by Segré and Silberberg [9], the concept was later applied by Di Carlo for particle focusing and separation in microchannels [10]. Inertial microfluidics utilizes the hydrodynamic effects that arise at finite Reynolds numbers to manipulate particles. Particles of different sizes follow distinct migration paths in flow fields created by specially designed microchannels, resulting in size-based separation. Di Carlo et al. demonstrated the separation of polystyrene particles of varying sizes (2 µm- 17 µm) using rectangular, square, and curved microchannels [11]. Kuntaegowdanahalli et al. employed an Archimedean spiral microchannel to separate 10 µm, 15 µm, and 20 µm polystyrene particles, achieving 90% separation efficiency [12]. Lee et al. explored a label-free method for separating cancer cells from white blood cells using inertial microfluidics in a contraction-expansion array [13]. The researchers used 10 and 15 μm particles as models for white blood cells (WBCs) and cancer cells, respectively, maintaining high cell viability. Numerous works can be found in the literature that utilize inertial microfluidics for the size-dependent isolation of CTCs from blood cells. However, recent research suggests that CTCs may display significant size overlap with WBCs. Studies by Marrinucci et al. [14] and Jin et al. [15] reported that CTCs in colorectal and prostate cancer patients exhibit considerable size overlaps with WBCs. Additionally, lung carcinoma epithelial cells, specifically A549 cells, show substantial size overlaps with WBCs. As a result, a high degree of WBC contamination may be present while isolating CTCs from blood cells in many of the devices mentioned earlier.

To address the limitations of individual cell separation techniques, hybrid devices integrating multiple techniques have emerged as promising solutions. These hybrid devices offer superior performance, versatility, and convenience. Hybrid devices are also capable to process multi-target cells, achieve multiplexed separation, provide higher sensitivity, and offer tunability across a wide operational range [7]. Chang and Cho combined DLD with DEP, replacing the mechanical pillar array with spot electrodes and creating a virtual DLD array using n-DEP force generated by an AC electrical field [16]. This method allows for tunable separation of particle sizes by adjusting the frequency and amplitude of the electric field. Aghaamoo et al. also combined DLD with DEP for the separation of CTCs from WBCs [17]. However, these DLD-DEP devices suffer from low throughput and may experience clogging. Dielectrophoretic Field-Flow-Fractionation is another method combining DEP and FFF for particle or cell separation, based on different densities, dielectric, and mechanical properties. Its batch-mode operation, however, limits throughput [18]. Yan et al. developed DEP-assisted hydrophoresis devices to levitate particles towards the top wall of the channel, enabling hydrophoretic ordering and size-based particle separation [19]. Moon et al. proposed a hybrid device that utilizes a multi-orifice flow fractionation (MOFF) channel and a DEP channel to isolate circulating tumor cells (CTCs) from blood [20]. The MOFF channel exploits inertial separation for high-throughput and high-yield filtration of blood cells, while the serially connected DEP sorter serves as a precise post-processor to further enhance separation efficiency and purity in a two-stage process. In contrast, Zhang et al. developed a DEP-coupled serpentine inertial microfluidic channel for particle separation by modulating electric voltages [21]. This technique is limited to separating particles with significant size differences, and its maximum lateral separation distance is constrained. More recently, Khan et al. and Islam et al. demonstrated high-throughput separation of cells using a serpentine, zigzag, and contraction-expansion array channel in conjunction with inertial microfluidics [22–24]. However, the high voltages used for particle separation in these devices may lead to electroporation or electrodestruction [25]. Furthermore, these approaches suffer from low separation distances, compromising cell separation precision, and are limited in their ability to separate CTCs from WBCs of specific types.

In this study, we report on a novel technique for label-free and high-throughput separation of CTCs from a heterogeneous mixture of WBC subtypes utilizing dielectrophoresis-assisted inertial migration in a spiral microchannel. To the best of our knowledge, no prior studies have been conducted on the separation of heterogeneous cell types with overlapping cell size utilizing interdigitated electrodes on a spiral microchannel geometry. A multi-physical model has been developed and validated in this work to investigate the performance of separation under various design configurations and flow conditions. Such a model can provide valuable information about the interactions between heterogeneous cell types, blood sample and buffer solutions with externally applied AC signals. This information on the physical phenomenon is needed to develop sensitive dielectrophoresis-assisted inertial migration in a curved channel. Designing sensitive interdigitated electrode arrays that can separate the desired cell type from the heterogeneous cell mixture at a large separation distance is critical, as larger separation distances also translate to better sensitivities which are much needed in the medical diagnosis. Unfortunately, there are no previous scientific investigations to address these questions. In the proposed method, planar interdigitated electrodes are embedded within a spiral microchannel for simplicity, rather than creating a two-stage separation device. The interdigitated electrodes offer significant advantages in mitigating the decline in metal electrode performance resulting from electrode fouling, a critical issue in traditional AC DEP devices. By employing the DEP force, cells are effectively separated based on their distinct dielectric properties, while the inertial forces simultaneously allow for high-throughput, continuous separation. The hybrid design addresses the size dependency issues found in traditional inertial microfluidics and surpasses conventional DEP devices by offering continuous high throughput separation without requiring complex parallel microfluidic channel layouts. Utilizing the unique channel design, we show that size-independent cell separation can be achieved at high throughput with a large separation distance and a low voltage through extensive numerical simulation. The effectiveness of the system is also demonstrated and discussed for the separation of lung cancer cells A549 from heterogenous WBC subtypes, including Granulocytes, Monocytes, T-lymphocytes and B-lymphocytes.

2 RELATED THEORY

Inertial microfluidics is characterized by lateral migration, which dictates the equilibrium positions of randomly distributed particles within a microchannel [9]. The resulting lateral migration of the particles in a curved microchannel operating at laminar flow with finite inertia is influenced by the combined effects of viscous drag force, wall-induced lift force, shear gradient lift force, and dean drag force [10]. Understanding the interplay between these forces is crucial for various applications, such as particle manipulation and cell separation. Firstly, viscous drag experienced by the particles causes them to accelerate and eventually reach the same velocity as the fluid along the flow direction. Furthermore, the lateral migration of particles in a microchannel is influenced by the combined action of two inertial forces: the wall-induced lift force and the shear gradient lift force. The wall-induced lift force originates from the disturbance of the flow field surrounding particles, prompting them to move from the wall toward the center of the channel. In contrast, due to the parabolic nature of the velocity profile at the finite inertia of the fluid, the particles experience a shear gradient lift force that drives them from the channel center toward the wall. The resultant force between these two forces is known as net inertial lift force that varies along the cross-section of the channel and can be expressed as[10]:

$$F_{Lift} = \frac{\rho_f U_m^2 a_p^4}{D_h^2} f_L(Re_c, z) \tag{1}$$

where ρ_f, U_m, a_p, D_h, and f_L is the fluid density, maximum velocity of the fluid, cell diameter, and hydraulic diameter of the channel and lift coefficient, respectively. For the fluid viscosity of μ_f, the Reynold number is given as:

$$Re_c = \frac{\rho_f U_m D_h}{\mu_f} \tag{2}$$

Due to the curvature of the spiral microchannel, a radially outward centrifugal force generates a secondary flow comprising two counter-rotating vortices, known as Dean vortices. The magnitude of these vortices can be determined for a curved channel with a radius of curvature R using a dimensionless number called the Dean number, expressed as follows [26]:

$$De = Re\sqrt{\frac{D_h}{2R}} \tag{3}$$

The Dean vortex enhances the lateral motion of cells across a channel and alters the positions of inertial focusing equilibrium. This is achieved by imposing a drag force that is proportional to the Dean flow velocity. The average Dean flow velocity is a function of the Dean number and can be expressed mathematically as [26]:

$$U_{dean} = 1.8 \times 10^{-4}\, De^{1.63} \tag{4}$$

Dielectrophoretic (DEP) force arises due to the interaction between nonuniform electric fields and the field-induced electrical polarization of cells. The time-averaged DEP force experienced by the cells when they are placed in an alternating electrical field can be expressed as [27]:

$$\boldsymbol{F_{DEP}} = 2\pi\varepsilon_{med}r^3 Re[K_{CM}(f)]\nabla|\boldsymbol{E}|^2 \tag{5}$$

where ε_{med}, r, f, and $|\boldsymbol{E}|$ is the permittivity of the suspension medium, radius of the particle, field frequency, and the root-mean-squared intensity of the applied electric field, respectively. In the equation, $Re[K_{CM}(f)]$ represents the magnitude of the real part of the Clausius-Mossotti (CM) factor which can be expressed as [28]:

$$K_{CM}(f) = \frac{\bar{\varepsilon}_{cell} - \bar{\varepsilon}_{med}}{\bar{\varepsilon}_{cell} + 2\bar{\varepsilon}_{med}} \tag{6}$$

where $\bar{\varepsilon}_{cell}$ and $\bar{\varepsilon}_{med}$ represent the complex permittivity of the cell and medium, respectively. At an electric field of angular frequency ω, and for permittivity and conductivity of ε and σ, respectively the complex permittivity can be expressed by the following equation [28]:

$$\bar{\varepsilon} = \varepsilon - j\frac{\sigma}{\omega} \tag{7}$$

The CM factor determines both the direction and magnitude of the DEP force exerted on particles. When $Re[K_{CM}(f)] > 0$, the particle experiences positive DEP and is attracted towards the electrodes due to its higher polarizability than the surrounding medium. Conversely, when $Re[K_{CM}(f)] < 0$, the particle experience negative DEP, where it has lower polarizability than the immersion medium and is repelled from the electrodes. From equation 6 and 7, it can be observed that the CM factor is reliant on the frequency of the applied electric field. Therefore, the DEP force experienced by a particle can be manipulated by selecting an appropriate frequency for the applied electric field. Between positive and negative DEP forces, there is a frequency at which a particle does not experience any DEP force where the $Re[K_{CM}(f)] = 0$, and this is known as the crossover frequency.

3 OPERATING PRINCIPLE

In this study, a novel electrode-embedded spiral microchannel is presented for the separation of CTCs from WBCs. Planar interdigitated electrodes with width and gap of 100 µm and 20 µm, respectively, are placed at the bottom of the microchannel. The spiral microchannel shown in Error! Reference source not found.**a** has a rectangular cross-section of width and height of 300µm x 100µm, respectively, and is created by merging an inner semi-circle with a diameter of 4.5mm and a spiral section with a parametric equation of $r = (4.5+\theta/\pi)$ mm, where θ ranges from π to 3.5π. The spiral channel is connected by a straight section measuring 3.5mm in length to two outlets, outer one designated for WBC collection and inner one for CTC collection. Additionally, the channel has two inlets. The outer inlet is used for introducing the WBCs and CTCs mixture, while the inner inlet is for injecting the sheath flow. The sheath flow is injected into the channel at twice the flow rate of the sample, ensuring that all particles are displaced toward the outer wall. An additional sheath flow is introduced through the top half of the outer inlet as shown in Error! Reference source not found.**b,** to push all particles towards bottom of the channel, a prerequisite for the removal of the top focusing position. The importance of this top sheath flow for the separation of cells has been investigated and subsequently discussed in the result section.

In the proposed methodology, when an AC electric field is not present, all cells are expected to migrate toward the inner wall of the curved microchannel while traversing the channel under the influence of dean drag and inertial lift forces. The introduction of an AC electric field generates a non-uniform electric field, which can exert a DEP force on the cells depending on their dielectric properties. DEP force is not expected to influence the trajectory of the CTCs at the cross-over frequency; on the other hand, by the action of the negative DEP force WBCs will be repelled by the interdigitated electrodes placed at the bottom of the channel. The interplay of the DEP force, in addition to the inertial-lift and dean-drag forces, determines the unique equilibrium positions of the WBCs and the CTCs, enabling the formation of distinct cell streams that can be collected at separate outlets.

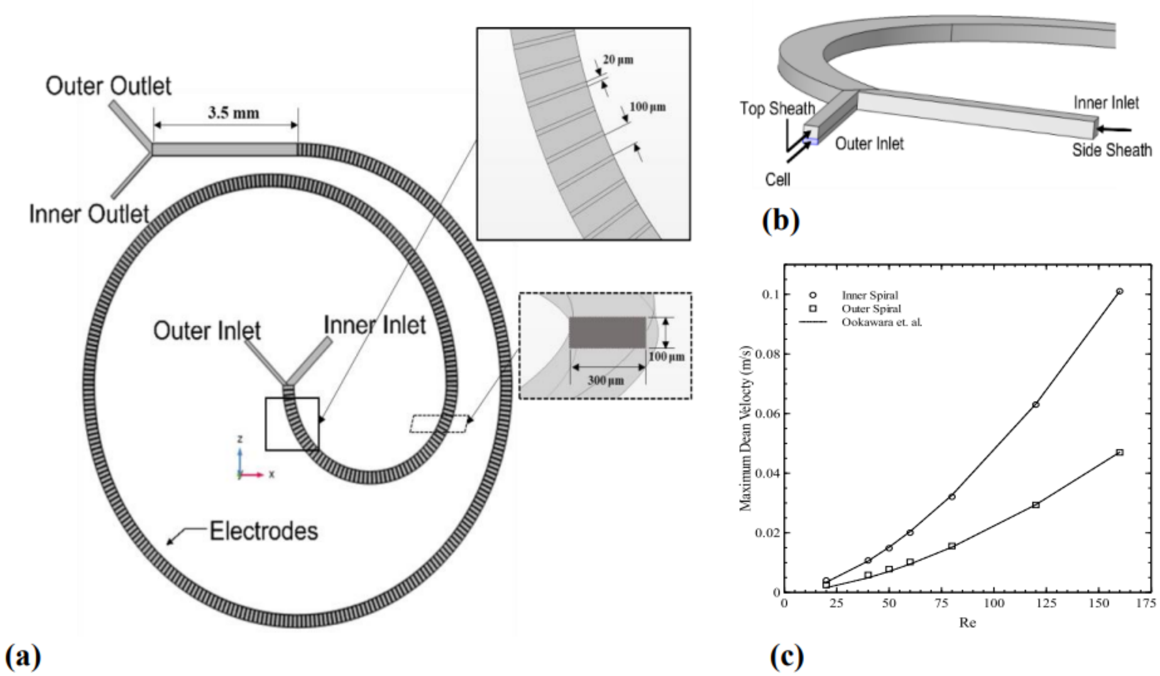

Figure 1. (a) Schematic of the electrode-embedded spiral channel. (b) The relative position of cells, top sheath and side sheath inlet have been shown. Cells and the top sheath have been injected through the outer inlet whereas the side sheath has been introduced through the inner inlet. (c) The simulation result obtained in our work has been validated against the experimental works existing in the literature. Dean velocity obtained in our study at different Reynolds numbers are in good agreement with the empirical relation proposed by Ookawara et. al. [26]

4 NUMERICAL MODELING

Numerical models are established in this work for analyzing flow patterns and cell trajectories utilizing the inertial-DEP method. The fluid flow and electric field are solved using the Laminar and AC/DC modules within COMSOL Multiphysics, respectively. To determine the velocity and pressure fields, in addition to the continuity equations, the following Navier-Stokes equation is used:

$$\rho\left(\frac{\partial \boldsymbol{U}}{\partial t}+\boldsymbol{U}\nabla\boldsymbol{U}\right)= -\nabla p+\eta\nabla^2\boldsymbol{U} \tag{8}$$

where $t, p,$ and η are time, pressure, and viscosity, respectively. The viscosity and density of the buffer solution are considered as 1000 kg/m^3 and 1.002 mPa.s respectively, same as deionized water. A fully developed fluid velocity profile is used for the inlet and no-slip and static pressure boundary conditions are applied to the walls and the outlet, respectively.

Additionally, the following set of equations is solved to obtain the electric field E:

$$\boldsymbol{E}= -\nabla\phi \tag{9}$$

$$\nabla.(\epsilon_m\boldsymbol{E})=\rho_E \tag{10}$$

$$\frac{\partial \rho_E}{\partial t} + \nabla . (\sigma \boldsymbol{E}) = 0 \tag{11}$$

where ϕ, ε_m, ρ_E and σ are the electric potential, medium permittivity, volumetric free charge density, and medium conductivity, respectively. Boundary conditions for the electrodes are set with electrical potentials ranging from a peak-to-peak voltage of 0 to 15V. Alternating positive and negative potentials are assigned to consecutive electrodes, with insulated boundary conditions implemented in the space between the electrodes.

After solving the velocity and the electric field, the particle tracing module is used to analyze the influence of the resultant field on the trajectory of the individual cells determined by the net forces acting on the particles. As the density of the medium (1000 kg/m^3) is close to the density of the cell (1070 kg/m^3), the sedimentation force is considered to be negligible. [29]. Other forces such as Brownian and Basset forces can also be ignored due to their negligible effects on the flow [30]. Consequently, the primary forces that are acting on the cells are the drag force, lift force, and DEP force. To determine the trajectory of the cells in an incompressible fluid, a transient solver is utilized that incorporates the above-mentioned forces as follows:

$$m_{cell} \frac{d}{dt}(U_{cell}) = \boldsymbol{F_{drag}} + \boldsymbol{F_{lift}} + \boldsymbol{F_{DEP}} \tag{12}$$

The drag force at an intermediate Reynolds number is computed utilizing the Schiller-Naumann drag model that accounts for the inertial effect of the drag force on a single spherical particle as given below:

$$F_{drag} = \left(\frac{1}{\tau_p}\right) m_{cell}(U - U_{cell}) \tag{13}$$

where the velocity response time, τ_p is defined as:

$$\tau_p = \frac{4\rho_p a_p^2}{3\mu C_d Re} \tag{14}$$

In this equation C_d represents drag coefficient and can be expressed as [31]:

$$C_d = \frac{24}{Re}(1 + 0.15Re^{0.687}) \tag{15}$$

To solve the transient numerical model, a fully coupled iterative GMRES solver is used with a convergence criterion of 10^{-3}. Ten cells of each type are released from the inlet at an interval of 2×10^{-5} s with injection starting from 0s. Bounce wall condition is applied at the wall for the cell particles. To avoid stiffness in the numerical solutions, an automatic time stepping method known as Generalized alpha has been utilized. The interval between the cell injection time was maintained to be a multiple of this time step. The total time for simulation is set to 0.5s which is determined by the time it takes for the particles to reach the outlet from the inlet.

The different components constituting an actual cell such as cytoplasm, nucleus, and cell membrane give rise to their inhomogeneity. To characterize this inhomogeneity single-shell model is used, with equivalent complex permittivity of the cell expressed as [32]:

$$\bar{\varepsilon}_{\text{cell}} = \bar{\varepsilon}_{\text{m}} \frac{\left(\frac{r}{r-d}\right)^3 + 2\left(\frac{\bar{\varepsilon}_{cyt} - \bar{\varepsilon}_{mem}}{\bar{\varepsilon}_{cyt} + \bar{\varepsilon}_{mem}}\right)}{\left(\frac{r}{r-d}\right)^3 - \left(\frac{\bar{\varepsilon}_{cyt} - \bar{\varepsilon}_{mem}}{\bar{\varepsilon}_{cyt} + \bar{\varepsilon}_{mem}}\right)} \tag{16}$$

where d is the cell membrane thickness, and the subscripts *cyt* and *mem* stands for cytoplasm and cell membrane, respectively. $\bar{\varepsilon}$ can be found from the Equation 7. Lung cancer cell A549 is chosen as the representative of CTCs. On the other hand, WBC can be mainly categorized into four categories: T-lymphocyte, B-lymphocyte, Monocyte, and Granulocytes. Different types of WBCs, their size, dielectric properties, cross-over frequency, and the approximate percentage in adults are given in Table 1[32–34]. Assuming a buffer conductivity of 0.055 S/m and a relative permittivity of 80, the cross-over frequency of the cell is evaluated from the computations of the real part of the CM factor using Equations 6 and 7 and the other dielectric properties of the cell listed in Table 1.

Table 1. Types of WBC, their size, dielectric properties, crossover frequency and the approximate percentage in adults

	T-lymphocytes	B-lymphocytes	Monocytes	Similar-sized WBC (Granulocytes)	CTC (A549)
Radius *(μm)*	3.29 ± 0.35	3.29 ± 0.26	4.63 ± 0.36	7± 1	6.9 ± 1.1
σ_{cyt} *(S/m)*	0.65	0.73	0.56	0.72	0.23
ε_{cyt}	104	154	127	111	100
σ_{mem} *(S/m)*	1×10^{-6}	1×10^{-6}	1×10^{-6}	1×10^{-6}	2×10^{-6}
ε_{mem}	5	5	5	5.54	9.4
Cross over frequency *(kHz)*	326	327	231	139	80
Percentage in adults	21	9	5	65	-

It can be seen from Table 1 that the crossover frequency of the CTCs (80 kHz) is always smaller than the crossover frequency of WBCs [35]. Given that the method proposed in this article relies on the combined effect of size and the relative difference in the crossover frequency of different cells for the separation, it can be expected to successfully separate CTCs from a mixture of WBCs. In the first part of this study, the working principle of the device and its effectiveness in separating overlapping-sized WBCs from CTCs is demonstrated using only one representative type of WBCs. Granulocytes, having size overlaps with CTCs and being the most abundant WBCs in the human body, were chosen for this purpose. Subsequently, the effectiveness of the model in separating CTCs from a mixture of WBCs is investigated.

5 VALIDATION

In this study, the numerical solutions for both velocity and electric field were independently validated against the existing literature. The flow model was verified by comparing the maximum dean velocity at different Reynolds numbers obtained in our simulations with the empirical relation proposed for curved channel by Ookawara et al. [26]. For this purpose, the spiral microchannel was assumed to consist of two circular sections with radii of 2.25cm and 4cm. In Error! Reference source not found.**c**, maximum dean velocities are represented by circle and square marks for the inner and outer spirals, respectively. It can be seen from the figure that, the numerical results align well with the empirical power law expressed by Equation 4 that has been proposed in [26].

To validate our methodology on electrical module of the simulation, we have compared our electric field distribution with the work of Zhang et. al. [36]. In Zhang's work, numerical simulations were used to augment the experimental results on particle separation using DEP force in a serpentine channel which is shown in **Fig. 2a**. To generate the figure, Zhang et. al. used a particle of 10μm diameter at $V_{p\text{-}p}$ of 45V and 1 MHz electric field frequency. The electric field contour in **Fig. 2b** is obtained from our simulation which shows close resemblance to the **Fig. 2a**. Additionally, a particle at 10μm from the bottom of the electrode is found to experience a maximum vertical DEP force of 1.6×10^{-7} N based on our simulation, which compares well with 1.68×10^{-7} N demonstrated in the work of Zhang et. al. [36].

A mesh sensitivity analysis is performed following the guideline presented by Roache [37] with three levels of mesh resolution. Comparing the two finer grids, the grid convergence index (GCI) is calculated using Eqn. 17. A GCI of 0.198% is obtained in our study with a safety factor of 1.25. Within 95% confidence interval, it can be stated that there is a negligible difference between the results obtained using elements of average size 0.0148mm and 0.0129mm grid with 523,734 and 781,080 elements, respectively. The grid study showed that with the current mesh setting the solutions of the numerical simulations that followed are independent of the grids [37].

$$GCI_{21} = F_s \frac{e_{21}}{r_{21}^{p} - 1} \qquad (17)$$

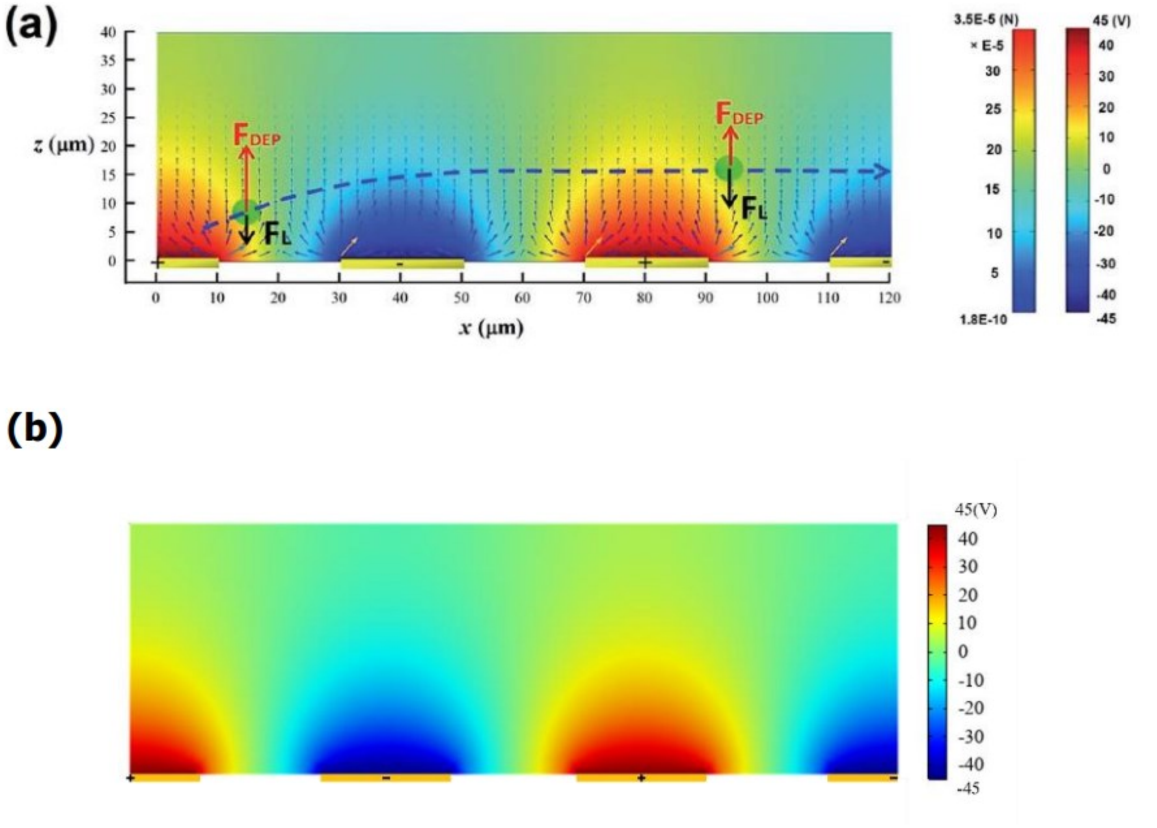

Figure 2. (a) The color map shows the electric field distributions within a longitudinal section of the channel at an electric field frequency of 1 MHz (a) Results from the work of Zhang et. al. [36] (b) Electric field contour obtained from our simulation.

6 RESULTS AND DISCUSSION

In hybrid inertial microfluidic devices, critical factors impacting the cell trajectories include flow regime, electric field intensity, and dielectric properties of both the sample and the buffer solution. This research delves into the effects of dielectrophoresis, sheath flow, and electrode arrangement on the separation efficacy of overlapping-sized cancer cells from healthy blood cells through numerical analysis, with the goal of identifying the most effective separation scenarios. Furthermore, by introducing a combination of four distinct white blood cell subtypes, the robustness of the system is assessed.

6.1 Influence of sheath flow and DEP on continuous CTC separation

This section elucidates the optimization of buffer inlet configurations and applied voltage in a hybrid spiral microfluidic channel, aiming to achieve efficient separation of CTCs from WBCs. In the hybrid spiral microfluidic channel equipped with interdigitated electrodes at the bottom, the non-uniform electric field intensity declines exponentially from the surface of the electrodes. Since the electric field weakens near the top of the channel, a sheath flow must be injected to eliminate the top focusing position of the cells and push them near the bottom for their successful separation. The inlet of the spiral microchannel with a height of 100μm was divided into two vertical sections:

the sheath and sample were introduced at the top and bottom sections, respectively, as depicted in Error! Reference source not found.**b**. To evaluate the impact of sheath flow ratios on cell separation characteristics, four inlet configurations were investigated. The first configuration involved no sheath flow. The other three configurations employed sheath inlet height to sample inlet height ratios of 1:3, 1:1, and 3:1. These configurations were investigated at zero and 10V, as depicted in **Figure 3**.

The results indicate that when no sheath flow was injected, and in the absence of DEP force at zero applied voltage, both the WBCs and CTCs focused at approximately 20 μm and 80 μm of the channel height. Consequently, two streams with identical cell mixtures were formed, showing no discernible separation, as illustrated in **Figure 3a**. At 10V, all the WBCs (denoted by red trajectories) moved to the top focusing position as they are acted upon by a negative DEP force and repelled away from the electrodes. In contrast, the CTCs (indicated by blue trajectories) were distributed evenly between the top and bottom focusing positions, maintaining their initial trajectory near the bottom of the channel, as shown in **Figure 3b**. Similar characteristics were observed when the sheath to sample height ratio is 1:3. These configurations do not produce distinct WBC and CTC streams, preventing effective cell separation.

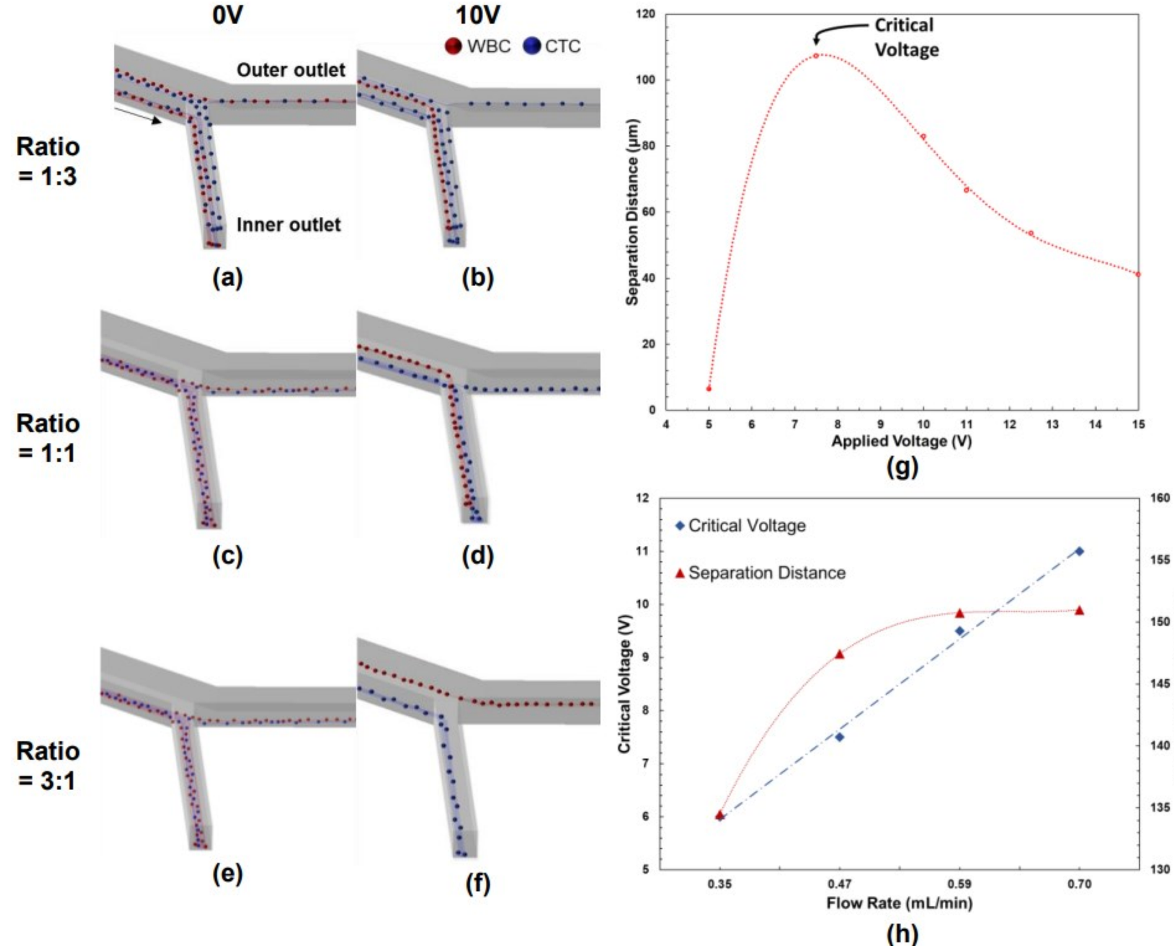

Figure 3. Effects of the top sheath flow and voltage on the trajectories of the cells. (a-f) The outlet positions of the cells with variation in the Sheath to Sample ratio of 1:3, 1:1, and 3:1 at an applied voltage of 0 and 10V. In these figures, the red stream represents the WBCs, and the blue stream represents the CTCs. (g)Variation in the lateral separation distance with applied voltage.

It can be seen that the lateral separation distance increases up to the critical voltage and then decreases again with any further increase in the voltage. (h) This critical voltage is dependent on the throughput, and the corresponding maximum separation distance that can be achieved at various flow rate is also shown in this figure.

At the sheath to sample height ratio of 1:1, more sheath was introduced at the inlet, and the cell mixture was pushed to the bottom half of the channel. In this configuration, without an electric field, only one focusing position for both cell types were found approximately 20 µm from the bottom of the channel, eliminating the top focusing position as shown in **Figure 3c**. At 10V, two distinct cell streams were formed where CTC maintain their initial trajectory at the bottom of the channel, whereas WBCs levitated towards the upper region of the channel as demonstrated in **Figure 3d**. Similarly, when the sheath to sample ratio is 3:1, vertical buffer flow inlet, and an applied voltage of 10V, the WBCs pushed upward. In contrast, the CTCs maintained their trajectory at the bottom of the channel, as shown in **Figure 3f**. In addition to the vertical levitation, the WBCs exhibit some lateral separation, which was further investigated and discussed in the following paragraphs. The separation distance is defined as the in-plane distance between the streams of the WBCs and the CTCs at the onset of the outlet. In the lateral direction, with 290 electrodes a considerable separation distance of 147 µm was obtained for a flow rate of 0.47mL/min corresponding to a Reynolds number of 40 in contrast to the vertical direction, where the maximum separation distance that can be achieved is limited by the channel height. Therefore, lateral migration has been utilized to collect CTCs and WBCs through different outlets, as demonstrated in **Figure 3f**, and the final configuration of the sheath to sample ratio is 3:1 has been chosen for the subsequent examination of cell migration characteristics in this work.

The lateral migration of WBCs between the inner and outer walls of the curved microchannel results in the formation of two distinct streams of WBCs and CTCs, which can be collected separately through the two designated outlets. The separation distance between these streams depends on the applied voltage. As previously discussed, in the absence of any electric field at 0V, both blood cells and cancer cells formed a single, indistinguishable stream and were collected through the same inner outlet, as shown in **Figure 3a**. As the applied voltage was increased, two separate cell streams emerged, where CTCs maintained their initial trajectory, whereas the WBCs experienced additional lateral displacement. The extent of this displacement increased with the applied voltage up to a voltage termed critical voltage, as illustrated in **Figure 3g**. For a throughput of 0.47mL/min, the maximum lateral separation distance was achieved at a critical voltage of 7.5V. Any further increase in voltage leads to a reduction in the lateral separation distance.

Variation in the separation distance and critical voltage with flow rate is demonstrated in **Figure 3h**. It can be seen that with the increase in the flow rate, the critical voltage increases, and the separation distance saturates at 151 µm at the flow rate of ~0.6 mL/min for 290 electrodes. Overall, it is found that in an electrode-embedded spiral microchannel, the ratio of the sheath flow inlet height to the channel height is a crucial parameter in determining the effectiveness of cell separation. To obtain a high-throughput separation of CTCs from WBCs, a top sheath flow must be employed to eliminate the top focusing position and the device can be operated at the critical voltage for the specified flow rate to achieve maximum separation.

6.2 Effects of the Number of Electrodes

The electric field significantly impacts the focusing positions of cells in a microchannel. In addition to the applied voltage of the electric field, the number and placement of electrodes are also crucial parameters that determine the final focusing position of the cells. To examine the effect of the number of electrodes on cell separation, various numbers of electrodes ranging from 60 to 416 were placed in different sections of the channel. In the investigation, 60 electrodes, at the critical voltage of 7.5V corresponding to a flow rate of 0.47mL/min and Reynolds number 40, resulted in the lowest lateral separation distance between particles. In this scenario, WBCs and CTCs shared similar trajectory and could not be separated at different outlets. Better separation was achieved by increasing the number of electrodes. It was found that the CTCs and the WBCs could only be collected at the different outlets when 100 or more electrodes were placed in the microchannel. **Figure 4a** and **Figure 4b** shows the state of the outlets and the DEP force experienced by the WBCs at 60 and 416 electrodes, respectively. It can be seen that although the time-averaged magnitude of the DEP force remained the same for both scenarios, the time and length over which cells experienced the DEP force increased with higher number of electrodes, as seen in **Figure 4a** and **Figure 4b**. **Figure 4c** demonstrates that better separation can be achieved using a higher number of electrodes. Notably, a larger separation distance of 202μm in a channel with width of 300 μm was achieved with 416 electrodes.

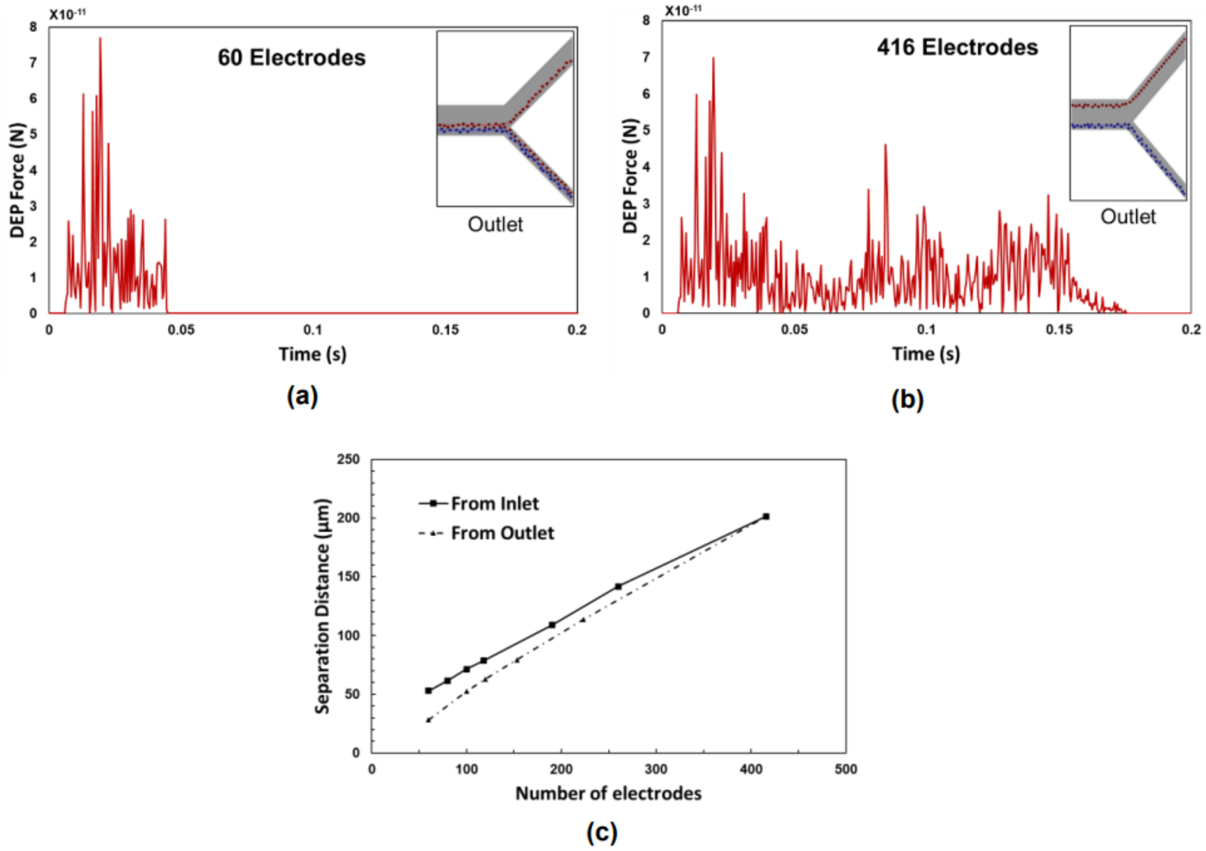

(a)

(b)

(c)

Figure 4. Variation in the separation distance of the cells achieved at the critical voltage corresponding to a Reynolds number of 40 for the different number of electrodes placed at the bottom of the spiral channel is shown in the figure. The DEP force experienced by the cells and the corresponding state of separation at the outlet for 60 and 416 electrodes is shown in figures (a) and (b), respectively. In these figures, the red stream represents the WBCs, and the blue stream represents the CTCs. No apparent separation can be observed with 60 electrodes whereas, it can be seen that, at the presence of 416 electrodes, WBCs experience DEP force for more time at greater length of the channel resulting in better separation. A lateral separation distance of 202 μm can be achieved with 416 electrodes. (c) A comparison of placing various number of electrodes from inlet and outlet is shown in the figure. It can also be seen that as the number of electrodes increases the separation distance increases and placing electrodes towards

the inlet results in better separation.

In addition to the number of electrodes, the placement of electrodes also impacted separation distance. **Figure 4c** shows larger separation distances were achieved when electrodes were placed near the inlet of the microchannel compared to the same number of electrodes placed toward the end as depicted by the solid and dashed lines in the figure, respectively.

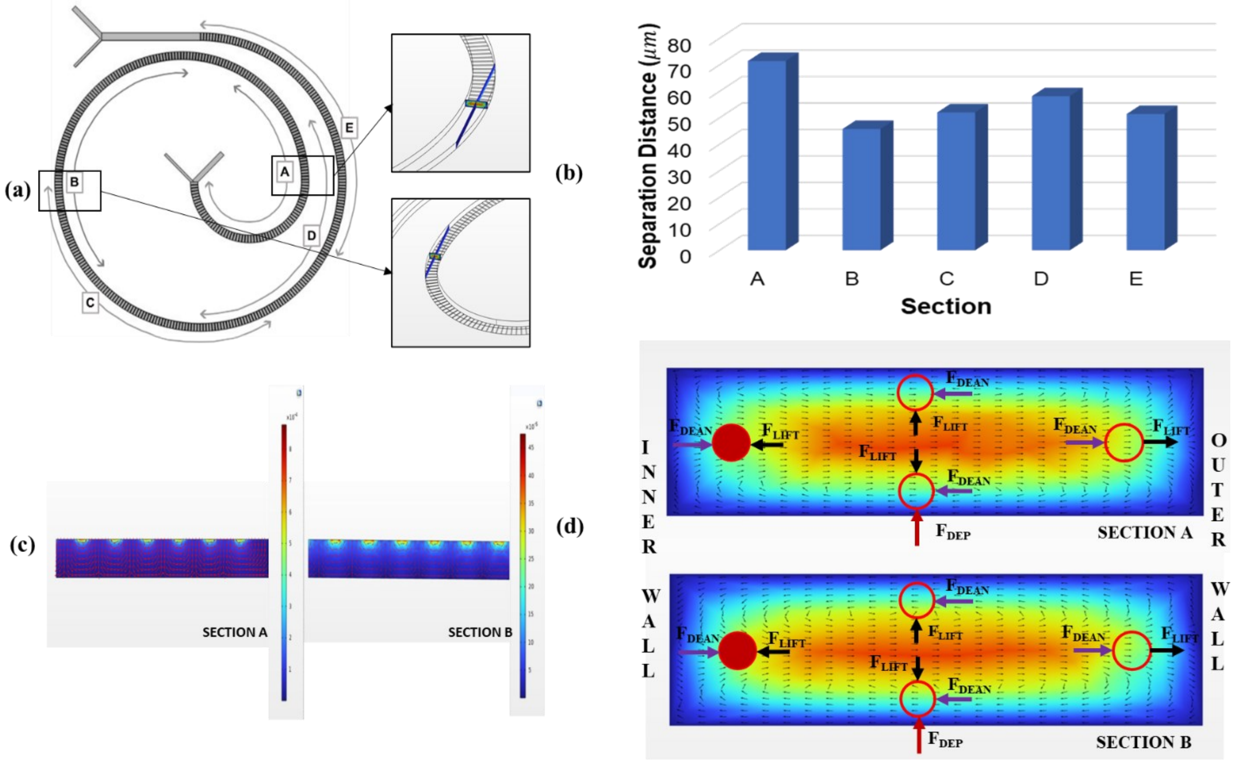

Figure 5. (a) 100 electrodes are placed at five different sections (A-E) of the spiral microchannel. (b) It can be seen from the bar chart in that highest separation distance can be achieved if the electrodes are placed in section A, nearest to the inlet. For the other four sections the separation distance is almost similar. (c) The comparison of electric field distribution in section A and section B. (d) The comparison of dean vortices between section A and section B with schematics indicating different forces acting on the particles. The vector lines represent dean vortices along the cross section of the flow direction. Four different positions of cells are shown pointing the forces acting at each location. The force balance on the cells is shown by using hollow and solid circular notations where hollow circular shape represents unbalanced cell positions. The cell position pointed by using solid red color shows the focusing position of the cells based on the force balance along the cross section of the spiral device.

Next, the channel was divided into five sections (A-E) at (A) the start of the channel, and at the angular position of (B) 1.5π, (C) 2π, (D) 2.5π and (E) towards the end as shown in **Fig. 5a**, with 100 electrodes placed in each of these sections, it was observed that the most effective separation occurred when the electrodes were placed near the inlet of the channel, as shown in **Fig. 5b.** 2D plots of the electric field simulations of the region for separation are given in **Fig. 5c** to show the corresponding electric field intensity distributions. As seen in the figure, the maximum electric field intensity is nearly 2 times stronger by placing the electrodes near the inlet, which is denoted as section A, in comparison to section B. 2D plots of the velocity vector distributions of the secondary Dean flow in two distinct locations boxed in **Fig. 5a** are also provided in **Fig. 5d** to illustrate the Dean flow patterns in sections A and B, along with schematics indicating different forces acting on the cells. It can be seen from the figure that the magnitude of the horizontal Dean force is larger towards the mid-plane when it is directed towards the outer wall. This means when the Dean force is dominating, cells at the top and bottom move laterally towards the inner wall, while cells closer to the mid-plane are pushed towards the outer wall. The Dean force, in addition to the wall induced and shear gradient lift forces, will make the focusing positions found in a straight channel unstable. When there is additional DEP force acting on the cells, it causes a further change in the cell equilibrium positions both laterally and vertically, resulting in different separation distances. As can be seen from **Fig.5b**, an average separation distance of 72 μm with just 100 electrodes was achieved when electrodes were placed near the beginning of the channel in section A, providing on average a 40% better separation compared to electrode placement in other sections. Some vital observation from this parametric study is that both the WBCs and the CTCs do not change their focusing position down the length of the channel where no electrodes are placed, and placing the electrodes towards the start of the channel results in the most effective separation of the particles. As expected, the electric field distribution plays an important role in the proposed design. When WBCs are lifted vertically upwards by a stronger DEP force, their lateral focusing position changes because of the complex force balancing leading to a more preferred location with a larger separation distance from CTCs in the proposed spiral microchannel. These results provide crucial insights into the placement of the electrodes for the fabrication, subsequently leading to efficient separation of the cells.

6.3 Effectiveness of the channel to separate CTCs from a mixture of WBCs

Finally, the ability of the inertial dielectrophoretic spiral microchannel to separate CTCs from various subtypes of WBCs was investigated. The investigation involved injecting different subtypes of cells, including the larger Granulocytes, into the channel and observing their trajectories in the absence and presence of an applied electric field. It was found that when no electric field was applied, no separation between cell types occurred, and all particles were located near the inner outlet of the channel (**6a**). In the presence of an electric field at the cross-over frequency of the CTCs, the different WBC subtypes experienced a negative DEP force, while the CTCs were unaffected. Consequently, the CTCs continued along their trajectory toward the inner wall of the channel. Applying an electric field at the critical voltage of Granulocytes caused Granulocytes and Monocytes to move from the bottom to the top focusing position of the channel, similar to the characteristics discussed in the

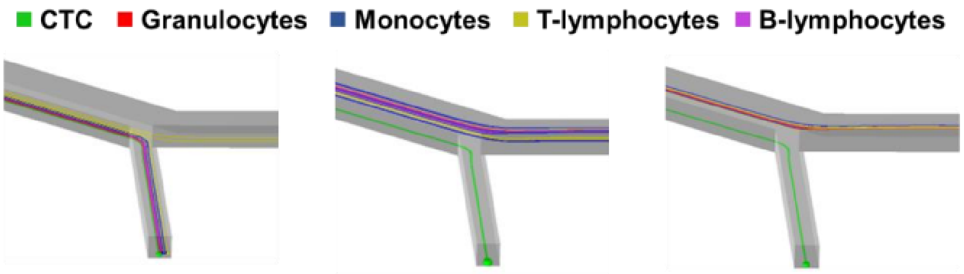

(a) 0V (b) 7.5V (c) 10V

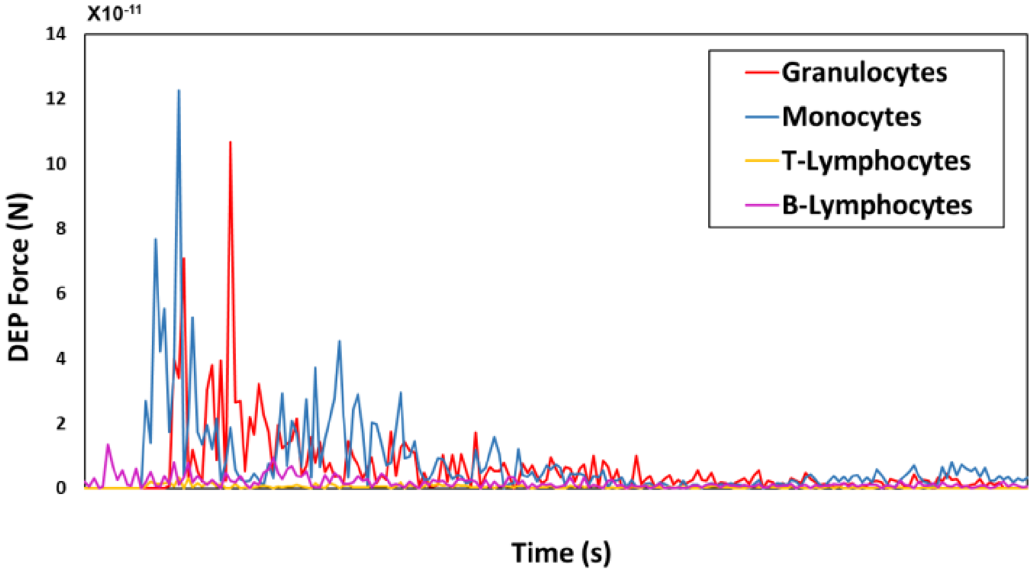

(d)

previous result section. This is illustrated in **6b**. Meanwhile, T-lymphocytes and B-lymphocytes occupy the lower focusing position of the channel.

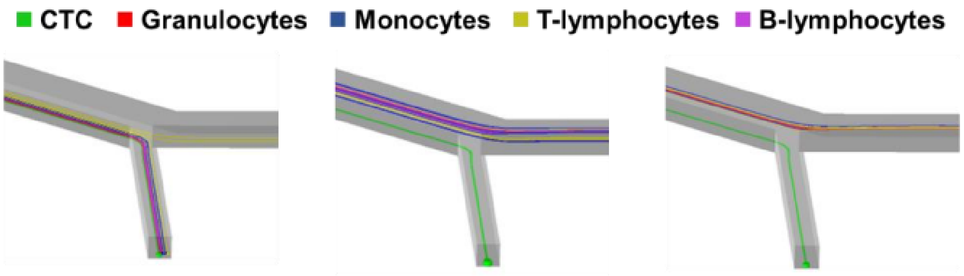

(a) 0V (b) 7.5V (c) 10V

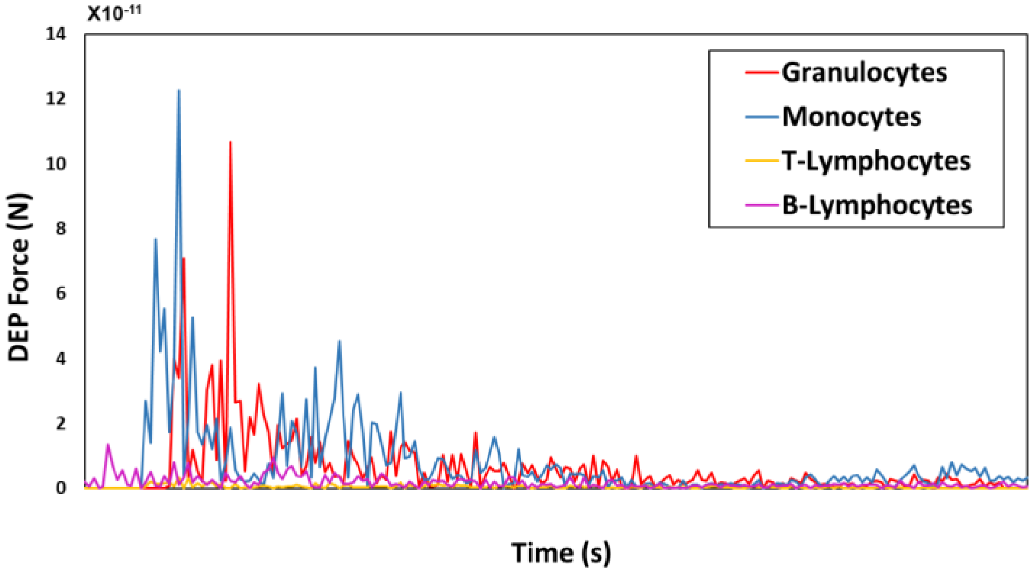

(d)

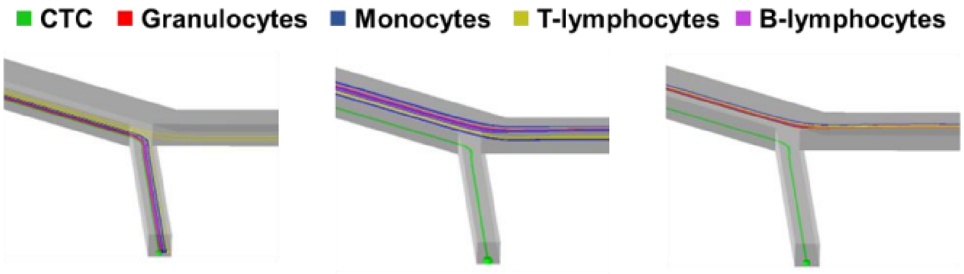

(a) 0V (b) 7.5V (c) 10V

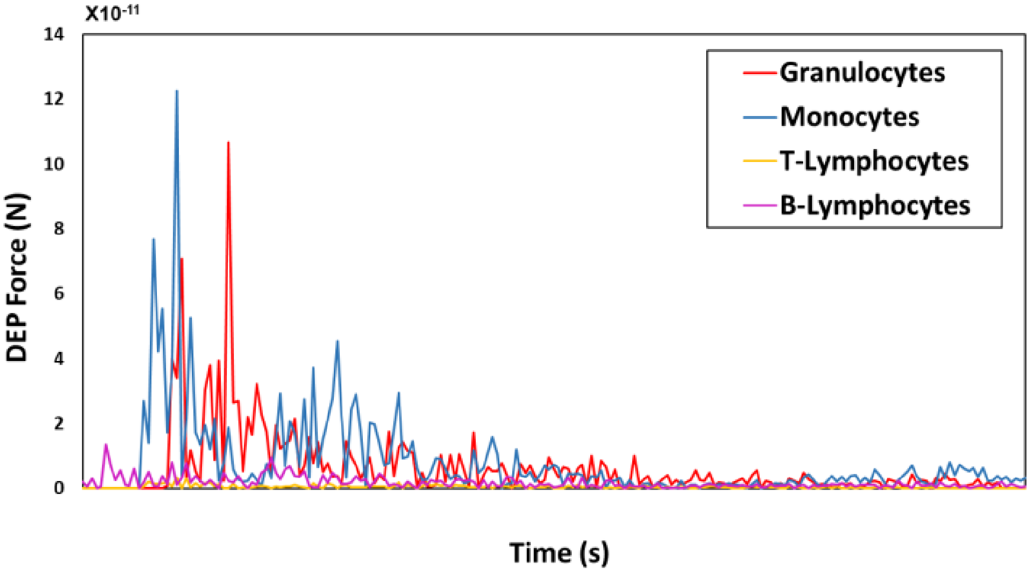

(d)

Figure 6. The spiral microchannel is able to separate CTCs from a mixture of WBCs with various sizes and dielectric properties in the presence of an electric field. (a) In the absence of any electric field all the cells follow the same trajectory (b) at the critical voltage of Granulocytes the other types of WBCs are also laterally separated and can be collected in a different outlet. (c) At voltage greater than the critical voltage all the different subtypes of WBCs occupy the top focusing position and also can be separated laterally. (d) The DEP force experienced by various sub types of WBC is shown in the figure. It can be seen that the magnitude of the DEP force experienced by Granulocytes and Monocytes are similar in magnitude whereas the T-lymphocytes and B-lymphocytes experience much lower DEP force.

In the presence of an electric field, all four WBC subtypes displayed sufficient lateral displacement to be successfully separated from the CTCs. This outcome can be attributed to the varying magnitudes of the inertial and DEP forces experienced by the different cells. Larger cells, such as CTCs and large WBCs, experience strong inertial lift forces dictated by equation 1. This causes the larger particles to focus tightly near the inner wall in the absence of any DEP force. At the same time, the smaller WBCs end up in the middle of the channel at the outlet and no separation was observed. When a non-uniform electric field was applied at the critical voltage of the Granulocyte, the CTCs maintained their trajectory and ended up at the inner outlet of the channel. In contrast, the WBCs experienced an additional DEP force that caused them to migrate from the inner to the outer wall of the channel.

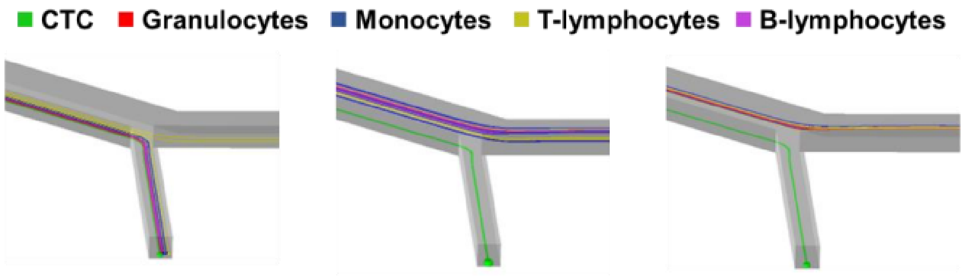

(a) 0V (b) 7.5V (c) 10V

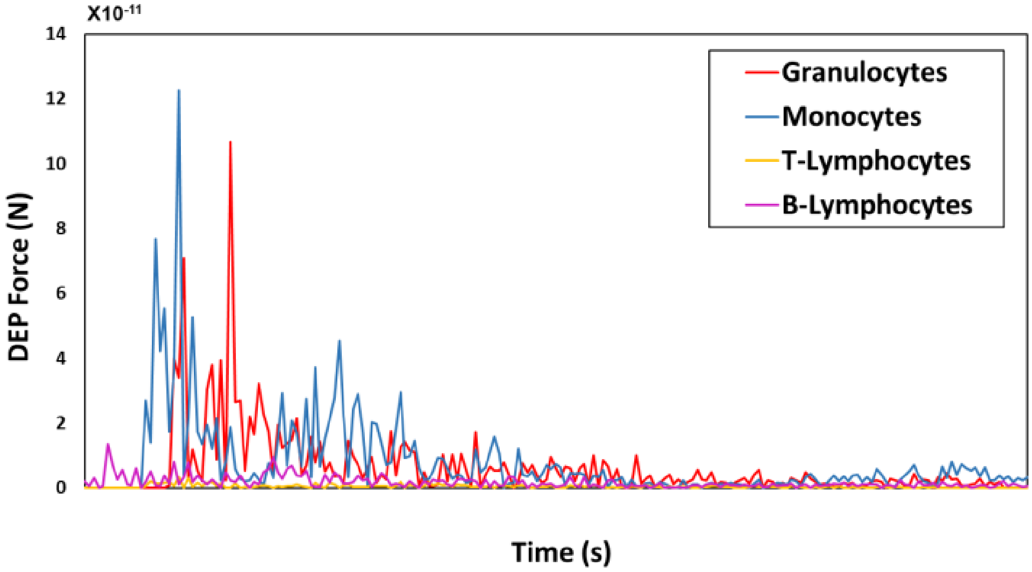

(d)

Through careful examination of the DEP force experienced by cells, as shown in **6d**, it can be observed that Granulocytes and Monocytes experience similar DEP force magnitudes, while T-lymphocytes and B-lymphocytes experience much lower DEP forces. The larger WBCs experience a strong DEP force that displaces them from the inner wall to the outer wall of the curved microchannel. On the other hand, the smaller WBCs experience a weaker DEP force, which on its own would not be sufficient for their migration towards the outer outlet of the channel. In addition to the weaker DEP force, these smaller cells also experience weaker inertial lift forces, as previously discussed. The weak inertial lift force allows the smaller cells to migrate under the influence of dean drag and continue flowing along the dean vortex and travel back towards the outer wall. Hence, both the large and the small WBCs can be collected at the outer outlet when an electric field is applied. From these observations, it can be concluded that T-lymphocytes and B-lymphocytes experience a lower DEP force and have a higher critical separation voltage compared to Granulocytes and Monocytes. However, these cells can still be effectively separated using inertial microfluidics within the spiral channel due to their smaller size, which makes them more susceptible to the dean vortex. Therefore, an electrode-embedded hybrid spiral microchannel is an ideal solution for separating CTCs from a mixture of different WBC subtypes, regardless of their size variations. The proposed device design is anticipated to have broad applicability across various cell lines, including breast cancer cell line MDA-MB-231 (with a characteristic crossover frequency of 42±6.8 kHz [33]), colon cancer cell line COLO205 (exhibiting a crossover frequency of 44.1±7.2 kHz [33]), kidney cancer cell line A498 (with a crossover frequency of 24.6±3 kHz [33]), and ovary cancer cell line OVCAR-3 (displaying a crossover frequency of 27±4.5 kHz [33]). Notably, all of these cell lines possess distinctly different crossover frequencies when compared to various WBC subtypes, including Granulocytes, Monocytes, T lymphocytes, and B lymphocytes.

7 CONCLUDING REMARKS

In conclusion, this study successfully demonstrates the potential of an electrode-embedded inertial dielectrophoretic microchannel for effective separation of CTCs from a mixture of WBCs regardless of the variations in size. In this study, optimizing sheath flow and DEP parameters showed that a sheath to sample height ratio of 3:1 and operation at the critical voltage provide the most effective cell separation. Moreover, investigating electrode configuration established that electrodes placed near the inlet of the microchannel results in better separation than same number of electrodes placed towards the end of the channel. With the maximum number of 416 electrodes embedded at the bottom of the spiral microchannel, a separation distance of 202 μm was achieved at the critical voltage of 7.5V. Furthermore, applying an electric field at the critical voltage enables sufficient migration for all four different subtypes of WBC (Granulocytes, Monocytes, T-lymphocytes, and B-lymphocytes) to be separated from CTCs. It was demonstrated that the successful isolation of smaller WBCs from CTCs primarily based on inertial forces, while the isolation of similar-sized CTCs and WBCs relies on dielectric properties and this size independent separation capability is uniquely enabled by the spiral microchannel. This novel cell sorting platform can be adapted for isolating specific target cells from complex mixtures, such as cell beads, by simply adjusting the applied electric field frequency without changing the channel design. Overall, the electrode-embedded hybrid spiral microchannel offers a promising and versatile solution for separating CTCs from a heterogeneous cell population, paving the way for advancements in cancer diagnosis, prognosis, and personalized medicine.

ACKNOWLEDGMENTS

X. L. Chen acknowledges the support from the National Science Foundation under grant NSF ECCS- 1917299.

CONFLICT OF INTEREST

The authors declare no conflict of interest.

DATA AVAILABILITY

The data that support the findings of this study are available from the corresponding author upon reasonable request.

8 REFERENCES

[1] Bankó, P., Lee, S. Y., Nagygyörgy, V., Zrínyi, M., Chae, C. H., Cho, D. H., Telekes, A. *J Hematol Oncol* 2019, *12*, 48.

[2] Budd, G. T., Cristofanilli, M., Ellis, M. J., Stopeck, A., Borden, E., Miller, M. C., Matera, J., Repollet, M., Doyle, G. V., Terstappen, L. W. M. M., Hayes, D. F. *Clinical Cancer Research* 2006, *12*, 6403–6409.

[3] Yang, C., Xia, B.-R., Jin, W.-L., Lou, G. *Cancer Cell Int* 2019, *19*, 341.

[4] Allard, W. J., Matera, J., Miller, M. C., Repollet, M., Connelly, M. C., Rao, C., Tibbe, A. G. J., Uhr, J. W., Terstappen, L. W. M. M. *Clinical Cancer Research* 2004, *10*, 6897–6904.

[5] Iv, C. W. S., D. Reyes, C., P. López, G. *Lab on a Chip* 2015, *15*, 1230–1249.

[6] Jacob, K., Sollier, C., Jabado, N. *Expert Review of Proteomics* 2007, *4*, 741–756.

[7] Dalili, A., Samiei, E., Hoorfar, M. *Analyst* 2019, *144*, 87–113.

[8] Gioe, E., Uddin, M. R., Kim, J.-H., Chen, X. *Micromachines* 2022, *13*, 661.

[9] Segré, G., Silberberg, A. *Nature 1961 189:4760* 1961, *189*, 209–210.

[10] Di Carlo, D. *Lab Chip* 2009, *9*, 3038.

[11] Carlo, D. D., Irimia, D., Tompkins, R. G., Toner, M. *Proceedings of the National Academy of Sciences of the United States of America* 2007, *104*, 18892–18897.

[12] Kuntaegowdanahalli, S. S., Bhagat, A. A. S., Kumar, G., Papautsky, I. *Lab on a Chip* 2009, *9*, 2973–2980.

[13] Lee, M. G., Choi, S., Kim, H.-J., Lim, H. K., Kim, J.-H., Huh, N., Park, J.-K. *Appl. Phys. Lett.* 2011, *98*, 253702.

[14] Marrinucci, D., Bethel, K., Lazar, D., Fisher, J., Huynh, E., Clark, P., Bruce, R., Nieva, J., Kuhn, P. *Journal of Oncology* 2010, *2010*, 1–7.

[15] Jin, C., M. McFaul, S., P. Duffy, S., Deng, X., Tavassoli, P., C. Black, P., Ma, H. *Lab on a Chip* 2014, *14*, 32–44.

[16] Chang, S., Cho, Y.-H. *Lab on a Chip* 2008, *8*, 1930–1936.

[17] Aghaamoo, M., Aghilinejad, A., Chen, X., Xu, J. *ELECTROPHORESIS* 2019, *40*, 1486–1493.

[18] Waheed, W., Sharaf, O. Z., Alazzam, A., Abu-Nada, E. *Journal of Chromatography A* 2021, *1637*, 461799.

[19] Yan, S., Zhang, J., Yuan, D., Li, W. *Electrophoresis* 2017, *38*, 238–249.

[20] Moon, H. S., Kwon, K., Kim, S. I., Han, H., Sohn, J., Lee, S., Jung, H. I. *Lab on a Chip* 2011, *11*, 1118–1125.

[21] Zhang, J., Yuan, D., Zhao, Q., Yan, S., Tang, S.-Y., Tan, S. H., Guo, J., Xia, H., Nguyen, N.-T., Li, W. *Sensors and Actuators B: Chemical* 2018, *267*, 14–25.

[22] Khan, M., Chen, X. *ELECTROPHORESIS* 2022, *43*, 879–891.

[23] Islam, M. S., Uddin, M. R., Chen, X. American Society of Mechanical Engineers Digital Collection, 2023.

[24] Islam, M. S., Chen, X. *Biotechnology Progress n/a*, e3341.

[25] Gascoyne, P. R. C., Shim, S. *Cancers* 2014, *6*, 545–579.

[26] Ookawara, S., Street, D., Ogawa, K. *Chemical Engineering Science* 2006, *61*, 3714–3724.

[27] Gasperis, G. D., Yang, J., Becker, F. F., Gascoyne, P. R. C., Wang, X.-B. *Micro¯uidic Cell Separation by 2-dimensional Dielectrophoresis*, 1999, *Vol*. 2.

[28] Kim, D., Sonker, M., Ros, A. *Analytical Chemistry* 2019, *91*, 277–295.

[29] Nieuwstadt, H. A., Seda, R., Li, D. S., Fowlkes, · J Brian, Bull, J. L., Nieuwstadt, H. A., Seda, · R, Li, · D S, Fowlkes, · J B, Bull, J. L. *Biomedical Microdevices 2010 13:1* 2010, *13*, 97–105.

[30] Khan, M., Chen, X. *ELECTROPHORESIS* 2022, *43*, 879–891.

[31] Yilmaz, F., Gundogdu, M. Y. *Korea-Australia Rheology Journal* 2009, *21*, 161–173.

[32] Cottet, J., Fabregue, O., Berger, C., Buret, F., Renaud, P., Frénéa-Robin, M. *Biophysical Journal* 2019, *116*, 12–18.
[33] Gascoyne, P. R. C., Shim, S., Noshari, J., Becker, F. F., Stemke-Hale, K. *Electrophoresis* 2013, *34*, 1042–1050.
[34] Prinyakupt, J., Pluempitiwiriyawej, C. *BioMedical Engineering Online* 2015, *14*, 1–19.
[35] S. Iliescu, F., Sim, W. J., Heidari, H., P. Poenar, D., Miao, J., Taylor, H. K., Iliescu, C. *ELECTROPHORESIS* 2019, *40*, 1457–1477.
[36] Zhang, J., Yan, S., Alici, G., Nguyen, N.-T., Di Carlo, D., Li, W. *RSC Adv.* 2014, *4*, 62076–62085.
[37] Roache, P. J. *Annu. Rev. Fluid. Mech* 1997, *29*, 123–60.

LIST OF FIGURES

Figure 1. (a) Schematic of the electrode-embedded spiral channel. (b) The relative position of cells, top sheath and side sheath inlet have been shown. Cells and the top sheath have been injected through the outer inlet whereas the side sheath has been introduced through the inner inlet. (c) The simulation result obtained in our work has been validated against the experimental works existing in the literature. Dean velocity obtained in our study at different Reynolds numbers are in good agreement with the empirical relation proposed by Ookawara et. al. [26]

Figure 2. (a) The color map shows the electric field distributions within a longitudinal section of the channel at an electric field frequency of 1 MHz (a) Results from the work of Zhang et. al. [36] (b) Electric field contour obtained from our simulation.

Figure 3. Effects of the top sheath flow and voltage on the trajectories of the cells. (a-f) The outlet positions of the cells with variation in the Sheath to Sample ratio of 1:3, 1:1, and 3:1 at an applied voltage of 0 and 10V. In these figures, the red stream represents the WBCs, and the blue stream represents the CTCs. (g)Variation in the lateral separation distance with applied voltage. It can be seen that the lateral separation distance increases up to the critical voltage and then decreases again with any further increase in the voltage. (h) This critical voltage is dependent on the throughput, and the corresponding maximum separation distance that can be achieved at various flow rate is also shown in this figure.

Figure 4. Variation in the separation distance of the cells achieved at the critical voltage corresponding to a Reynolds number of 40 for the different number of electrodes placed at the bottom of the spiral channel is shown in the figure. The DEP force experienced by the cells and the corresponding state of separation at the outlet for 60 and 416 electrodes is shown in figures (a) and (b), respectively. In these figures, the red stream represents the WBCs, and the blue stream represents the CTCs. No apparent separation can be observed with 60 electrodes whereas, it can be seen that, at the presence of 416 electrodes, WBCs experience DEP force for more time at greater length of the channel resulting in better separation. A lateral separation distance of 202 µm can be achieved with 416 electrodes. (c) A comparison of placing various number of electrodes from inlet and outlet is shown in the figure. It can also be seen that as the number of electrodes increases the separation distance increases and placing electrodes towards the inlet results in better separation.

Figure 5. (a) 100 electrodes are placed at five different sections (A-E) of the spiral microchannel. (b) It can be seen from the bar chart in that highest separation distance can be achieved if the electrodes are placed in section A, nearest to the inlet. For the other four sections the separation distance is almost similar. (c) The comparison of electric field distribution in section A and section B. (d) The comparison of dean vortices between section A and section B with schematics indicating different forces acting on the particles. The vector lines represent dean vortices along the cross section of the flow direction. Four different positions of cells are shown pointing the forces acting at each location. The force balance on the cells is shown by using hollow and solid circular notations where hollow circular shape represents unbalanced cell positions. The cell position pointed by using solid red color shows the focusing position of the cells based on the force balance along the cross section of the spiral device.

Figure 6. The spiral microchannel is able to separate CTCs from a mixture of WBCs with various sizes and dielectric properties in the presence of an electric field. (a) In the absence of any electric field all the cells follow the same trajectory (b) at the critical voltage of Granulocytes the other types of WBCs are also laterally separated and can be collected in a different outlet. (c) At voltage greater than the critical voltage all the different subtypes of WBCs occupy the top focusing position and also can be separated laterally. (d) The DEP force experienced by various sub types of WBC is shown in the figure. It can be seen that the magnitude of the DEP force experienced by Granulocytes and Monocytes are similar in magnitude whereas the T-lymphocytes and B-lymphocytes experience much lower DEP force.

LIST OF TABLES

Table 1. Types of WBC, their size, dielectric properties, crossover frequency and the approximate percentage in adults

	T-lymphocytes	B-lymphocytes	Monocytes	Similar-sized WBC (Granulocytes)	CTC (A549)
Radius *(μm)*	3.29 ± 0.35	3.29 ± 0.26	4.63 ± 0.36	7± 1	6.9 ± 1.1
σ_{cyt}*(S/m)*	0.65	0.73	0.56	0.72	0.23
ε_{cyt}	104	154	127	111	100
σ_{mem}*(S/m)*	1×10^{-6}	1×10^{-6}	1×10^{-6}	1×10^{-6}	2×10^{-6}
ε_{mem}	5	5	5	5.54	9.4
Cross over frequency *(kHz)*	326	327	231	139	80
Percentage in adults	21	9	5	65	-